

Article

## Magnetism-Structure Correlations during the $\epsilon \rightarrow \tau$ Transformation in Rapidly-Solidified MnAl Nanostructured Alloys

Felix Jiménez-Villacorta <sup>1</sup>, Joshua L. Marion <sup>1</sup>, John T. Oldham <sup>1</sup>, Maria. Daniil <sup>2</sup>, Matthew A. Willard <sup>2</sup> and Laura H. Lewis <sup>1,\*</sup>

<sup>1</sup> Department of Chemical Engineering, Northeastern University, 360 Huntington Ave., Boston, MA 02115, USA; E-Mails: fjv2003@gmail.com (F.J.-V.); marion.jo@husky.neu.edu (J.L.M.); jtoldham10@gmail.com (J.T.O.)

<sup>2</sup> Department of Materials Science and Engineering, Case Western Reserve University, Cleveland, OH 44106-7204, USA; E-Mails: mx421@case.edu (M.D.); maw169@case.edu (M.A.W.)

\* Author to whom correspondence should be addressed; E-Mail: lhlewis@neu.edu; Tel.: +1-617-373-3419.

Received: 13 December 2013; in revised form: 14 January 2014 / Accepted: 16 January 2014 / Published: 21 January 2014

---

**Abstract:** Magnetic and structural aspects of the annealing-induced transformation of rapidly-solidified Mn<sub>55</sub>Al<sub>45</sub> ribbons from the as-quenched metastable antiferromagnetic (AF)  $\epsilon$ -phase to the target ferromagnetic (FM)  $L1_0$   $\tau$ -phase are investigated. The as-solidified material exhibits a majority hexagonal  $\epsilon$ -MnAl phase revealing a large exchange bias shift below a magnetic blocking temperature  $T_B \sim 95$  K ( $H_{ex} \sim 13$  kOe at 10 K), ascribed to the presence of compositional fluctuations in this antiferromagnetic phase. Heat treatment at a relatively low annealing temperature  $T_{anneal} \approx 568$  K (295 °C) promotes the nucleation of the metastable  $L1_0$   $\tau$ -MnAl phase at the expense of the parent  $\epsilon$ -phase, donating an increasingly hard ferromagnetic character. The onset of the  $\epsilon \rightarrow \tau$  transformation occurs at a temperature that is  $\sim 100$  K lower than that reported in the literature, highlighting the benefits of applying rapid solidification for synthesis of the rapidly-solidified parent alloy.

**Keywords:** nanostructured magnetic materials; Mn-based magnets; rapid-solidification

---

## 1. Introduction

Current market and supply pressures on rare earth elements—components of technologically important advanced permanent magnets—are driving investigation into magnetic materials that can replace rare-earth-based alloys with more abundant and less strategically important elements. A promising strategy for realization of new concepts in permanent magnetic materials is to revisit the “classic” hard magnetic alloys that were widely used before the advent of the rare-earth-based supermagnets [1,2] and, by employing advanced fabrication and analysis methods, gain insight into the fundamentals governing their structure-magnetic property behavior for improved performance. Among the list of materials targeted for this purpose include intermetallic ferromagnetic Mn-based alloys, such as MnAl [3,4] or MnBi [5,6], which were considered as permanent magnet candidates in the 1960s and 1970s [7–9]. In particular, the MnAl compound with the tetragonal  $L1_0$  type crystal structure ( $\tau$  phase) combines favorable aspects, such as low density, large corrosion resistance, and low cost [10,11], with good permanent magnetic performance. The MnAl magnetic properties include a Curie temperature of  $T_C \sim 525$  K, a robust magnetocrystalline anisotropy,  $K_1 \sim 10^6\text{--}10^7$  J/m<sup>3</sup> ( $K_1 \sim 10^7\text{--}10^8$  erg/cm<sup>3</sup>) that fosters appreciable room-temperature coercivity values,  $H_c \sim 0.15$  to 0.4 T ( $H_c \sim 1.5$  to 4.0 kOe), and a relatively large saturation magnetization of  $M_s \sim 88\text{--}98$  emu/g that has enabled experimentally-realized maximum energy products of  $(BH)_{\max} \sim 16\text{--}56$  kJ/m<sup>3</sup> ( $(BH)_{\max} \sim 2\text{--}7$  MGOe) [12,13]. While some success has been recently achieved in the development of these materials [3,14,15] experience demonstrates that optimization of the microstructure and the magnetic features of new magnetic materials may take several years (or even decades) [4], making a strong case for renewed investigation of structure-property relationships in former generations of magnetic materials [16–18].

Non-equilibrium processing techniques, such as melt-spinning, splat-quenching, and mechanical milling, allow access to thermodynamically metastable phases and microstructures that can be beneficial, including nanoscaled features and enhanced magnetic properties [19,20]. Within the Mn-Al phase diagram, the ferromagnetic (FM)  $\tau$ -MnAl phase forms via a two-step reaction process that originates from the parent hexagonal  $\epsilon$ -MnAl phase through the intermediate  $B19$ -structured  $\epsilon'$ -phase, by annealing at temperatures in the range 723–823 K [21,22]. These transformations are assumed to be compositionally invariant, controlled by nucleation and growth processes [11,23] that commence at the grain boundaries [24,25]. Hence, MnAl fabrication methods that provide a refined microstructure with small  $\epsilon$ -crystallites are envisioned to yield enhanced surface-to-volume ratios that promote formation of the  $\tau$ -phase, with lowered phase transformation energy barriers and lower values for the transformation temperatures. Recent reports on  $\epsilon$ -phase MnAl thin films (5 nm thickness) [26,27] and on  $\epsilon$ -phase MnAl ultrafine nanocrystallites ( $\sim 8.2$  nm) obtained by mechanical milling [28] reveal an  $\epsilon \rightarrow \tau$  transformation temperature in the range  $\sim 623\text{--}673$  K, confirming the hypothesis that the temperature required for  $\tau$ -phase formation is dependent on details of the microstructure.

In this work, the annealing-induced evolution of magnetic and structural properties of nanostructured, rapidly-solidified  $Mn_{55}Al_{45}$  are evaluated at early stages of the  $\epsilon$ -MnAl to  $\tau$ -MnAl transformation confirmed to begin at  $T \sim 568$  K (295 °C), 50–100 degrees lower than previously-reported transformation onset temperatures. The evolution of the magnetic parameters of these heat-treated MnAl ribbons is correlated with phase transformation and microstructural attributes.

Clarification of the character of the  $\varepsilon \rightarrow \tau$  transformation is anticipated to lead to tailoring of existing pathways, or identification of new pathways, for stabilization of the  $L1_0$ -type  $\tau$ -phase, enabling the application of advanced processing methods, and associated improved performance as a rare-earth-free permanent magnetic material.

## 2. Experimental Section

Arc-melted ingots of nominal composition  $Mn_{55}Al_{45}$  made from initial charges of Mn granules (Alfa Aesar, 99.98% purity, metals basis) and Al foil (Alfa Aesar, 99.9% purity, metals basis) were used as precursors for melt-spinning under a He atmosphere at a pressure of 0.3 atm, with a tangential velocity of 64 m/s. The rapidly-quenched alloys produced by this process were shiny, brittle, approximately 50  $\mu\text{m}$  thick, and 1 to 5 cm in length. The average composition of the as-solidified ribbons was determined to within about 2 at.% using scanning electron microscopy—energy-dispersive X-ray spectroscopy (SEM–EDX; Hitachi S4800, Dallas, TX, USA). Crystal structures were confirmed with X-ray diffraction (XRD; Philips PANalytical X’Pert-Pro, Westborough, MA, USA) using  $\text{Cu-K}\alpha$  radiation. The  $\text{K}\alpha_2$  contribution to the diffracted X-rays was removed by a software-based correction algorithm. Lattice parameters were calculated with a least-squares cell parameter program [29], and crystallite sizes were determined from the Scherrer equation [30]. The phase transformation character of the alloy was investigated using Differential Scanning Calorimetry (DSC; Netzsch STA 449, Burlington, MA, USA) under an Ar atmosphere using heating rates of 5 K/min.

Annealing procedures were performed on samples of the as-quenched  $Mn_{55}Al_{45}$  alloy sealed in thin vitreous silica tubes under a vacuum pressure of  $1 \times 10^{-6}$  Torr to protect against oxidation. Two samples were placed at the same location in the center zone of a programmable tube furnace (MTI GSL1100X, Richmond, CA, USA) and simultaneously annealed in sequential 30-min intervals in the nominal temperature range  $373 \text{ K} \leq T_{\text{anneal}} \leq 618 \text{ K}$  (the actual  $T_{\text{anneal}}$  was within 2 K of the target value). After each heat treatment interval, the magnetic properties of one of the vacuum-sealed sample were analyzed. Magnetic measurements were carried out using a superconducting quantum interference device magnetometer (SQUID; Quantum Design MPMS, San Diego, CA, USA). Zero-field-cooling–field-cooling (ZFC-FC) magnetization *vs.* temperature curves ( $M$  *vs.*  $T$ ) were collected in the temperature range  $10 \text{ K} < T < 400 \text{ K}$ , using a probe field of 0.1 T. Magnetization loops ( $M$  *vs.*  $H$ ) were collected between 10 K and 300 K under ZFC and FC conditions (applied field during cooling:  $H_{\text{FC}} = 5 \text{ T}$ ). All magnetization measurements were corrected for demagnetization effects; each specimen was approximated as a cylinder and the demagnetization factor ( $N_d$ ) was determined from the plot of  $N_d$  *vs.* sample aspect ratio [31]. After observation of a significant variation in the magnetic features of the first sample, which occurred at  $T_{\text{anneal}} = 568 \text{ K}$  (295 °C), the first sample was removed from the silica tube for XRD investigation. Thermal treatment and magnetic examination procedures continue with the second sample up to  $T_{\text{anneal}} = 618 \text{ K}$  (345 °C); after this annealing step this second sample was removed from the silica tube and subjected to XRD examination to obtain phase and crystal structure information.

As discussed more thoroughly in Section 3, magnetic hysteresis loops obtained from the samples often indicated the presence of more than one magnetic phase. Contributions from different magnetic

components were extracted from the hysteresis curves collected at 10 K and at 300 K, using an empirical equation that describes the magnetization response of a ferromagnetic (FM) sample comprised of  $n$  independently-switching magnetic phases [32]:

$$M(H) = \sum_{i=1}^n \frac{2x_i M_s}{\pi} \tan^{-1} \left[ \left( \frac{H \pm H_{ci}^{(i)}}{H_{ci}^{(i)}} \right) \tan \left( \frac{\pi S^{(i)}}{2} \right) \right] \quad (1)$$

where  $M$  = total magnetization (emu/g),  $H$  = effective internal magnetic field (Oe),  $M_s$  = total saturation magnetization of the multi-phase material (emu/g),  $H_{ci}^{(i)}$  = effective intrinsic coercivity of magnetic phase-( $i$ ) (Oe),  $S^{(i)} = M_r^{(i)} / M_s^{(i)}$  squareness ratio (remanence vs. saturation; unitless),  $x_i$  = relative fractional contribution of each constituent magnetic phase respect to the total magnetization ( $x_i = M_s^{(i)} / M_s$ ), and  $n$  = number of constituent magnetic phases contributing to  $M$  (unitless).

### 3. Results

Melt-spun  $\text{Mn}_{55}\text{Al}_{45}$  ribbons analyzed by XRD (Figure 1) reveal a majority hexagonal ( $hcp$ ) phase, identified as  $\epsilon$ -MnAl [28,33]. As reported in detail elsewhere [34], each  $hcp$   $\epsilon$ -MnAl Bragg peak occurs in pairs, consistent with the presence of two phases with the  $\epsilon$ -MnAl crystal structure, denoted as  $\epsilon_1$  and  $\epsilon_2$ , with similar unit cell lattice parameters around  $a \sim 2.70 \text{ \AA}$  and  $c \sim 4.37 \text{ \AA}$  and identical  $c/a$  ratios  $\sim 1.62$ . The  $\epsilon_1$  and  $\epsilon_2$  phases possess unit cell volumes of  $V \sim 82.9 \pm 0.3 \text{ \AA}^3$  and  $V \sim 82.1 \pm 0.5 \text{ \AA}^3$ , respectively, and average crystallite sizes ( $D_\epsilon$ ) of approximately 30 and 60 nm, as calculated from the Scherrer formula (Figure 2). Therefore, the  $\epsilon_1$  phase has a larger unit cell with a significantly smaller grain size than the  $\epsilon_2$  phase. The remaining minority Bragg peaks in the XRD pattern are associated with a rhombohedral  $\gamma_2$ -MnAl phase with lattice parameters  $a = 10.1 \pm 0.2 \text{ \AA}$ ,  $b = 7.63 \pm 0.2 \text{ \AA}$ ,  $c = 16.0 \pm 0.3 \text{ \AA}$ , and unit cell volume  $V \sim 1230 \pm 40 \text{ \AA}^3$ .

**Figure 1.** XRD patterns from  $\text{Mn}_{55}\text{Al}_{45}$  as-spun ribbons and those annealed at 568 K and 618 K.

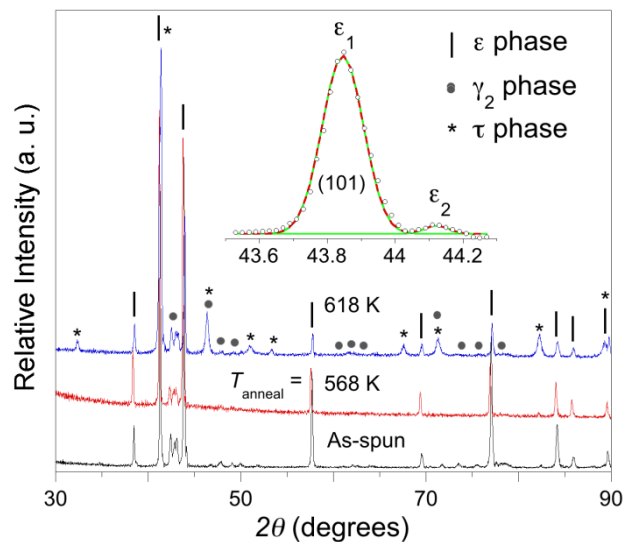
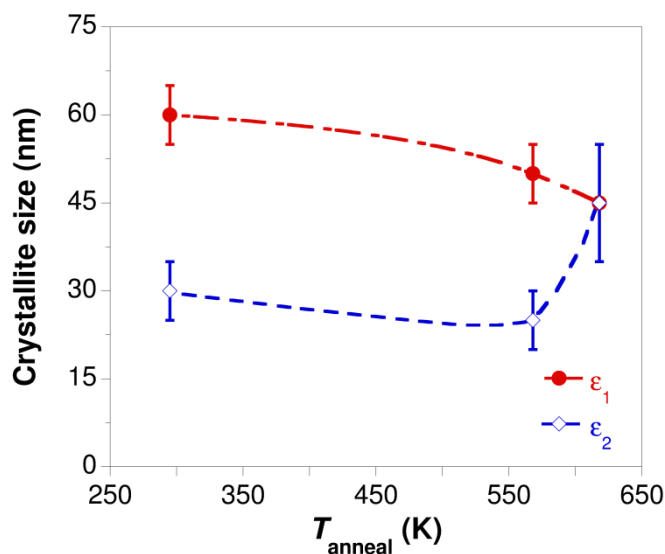


**Figure 2.** Thermal evolution of crystallite size ( $D$ ) of both hexagonal  $\varepsilon$ -MnAl regions— $\varepsilon_1$  (filled circles) and  $\varepsilon_2$  (open diamonds)—in melt-spun  $\text{Mn}_{55}\text{Al}_{45}$  ribbons. Dashed lines drawn between markers to guide eye.



The coherently-diffracting size of the *hcp*  $\varepsilon$ -phases in the  $\text{Mn}_{55}\text{Al}_{45}$  ribbons varies only slightly with annealing to  $T_{\text{anneal}} = 568$  K, and then reaches similar values ( $D_{\varepsilon} \sim 45$  nm) upon heating to 618 K. This result is consistent with the  $\varepsilon_1$  phase growing at the expense of the  $\varepsilon_2$  phase with annealing. At the higher annealing temperature an additional phase identified as the metastable tetragonal  $\tau$ -MnAl phase with  $L1_0$ -type structure is visible in the X-ray diffraction scans. The  $\tau$ -phase possesses unit cell lattice parameters  $a = 2.77 \pm 0.01$ ,  $c = 3.56 \pm 0.01$  Å, unit cell volume  $V = 27.3 \pm 0.1$  Å<sup>3</sup>, in close agreement with previous literature [8,14,28], and approximate crystallite size  $D_{\tau} \sim 20$  nm.

The magnetic response of the melt-spun MnAl alloys is also modified by annealing. The ZFC-FC  $M(T)$  curves of the as-quenched material (Figure 3) exhibit a cusp at  $T_{\text{peak}} = 95$  K, with a divergence in the magnetization for  $T < T_{\text{peak}}$  that is associated with the Néel temperature of the AF  $\varepsilon$ -phase [35]. Both, the cusp and the magnetization divergence, vanish with annealing to  $T_{\text{anneal}} = 618$  K, accompanied by a significant increase of the magnetization. Field-cooled hysteresis curves measured from the as-spun ribbons at  $T = 10$  K (Figure 4a) display a prominent shift along the applied field axis of  $H_{\text{ex}} \sim 1.3$  T ( $H_{\text{ex}} \sim 13$  kOe). The field-axis shift, not present under ZFC conditions, decreases with increased measurement temperature  $T$  and vanishes for  $T \geq T_{\text{peak}}$ . Further, it is noted that the hysteresis loops displayed in Figure 4a feature a small step at low fields in the ascending and descending branches of the curves, indicative of a lower-coercivity  $H_{\text{ci}} \sim 0.15$  T ( $H_{\text{ci}} \sim 1.5$  kOe) phase present in the sample in addition to the majority high-coercivity phase,  $H_{\text{ci}} \sim 1.9$  T ( $H_{\text{ci}} \sim 19$  kOe) phase. Subsequent annealing at moderate temperatures (see hysteresis loop for the  $T_{\text{anneal}} = 568$  K sample in Figure 4a) yields a decrease of the hysteresis loop shift previously noted at low temperature, accompanied by an increased magnitude of the second phase magnetization at room temperature (Figure 4b). Further annealing suppresses the contribution corresponding to the shifted hysteresis loop, and only the second phase is observed at both  $T = 10$  and 300 K, revealing an increased coercivity at both temperatures to a value of  $H_{\text{ci}} \sim 0.25$  T ( $H_{\text{ci}} \sim 2.5$  kOe).

**Figure 3.**  $M$  vs.  $T$  curves collected under a probe field of 1 kOe from as-spun  $Mn_{55}Al_{45}$  ribbons (filled circles) and those treated at 618 K (open diamonds).

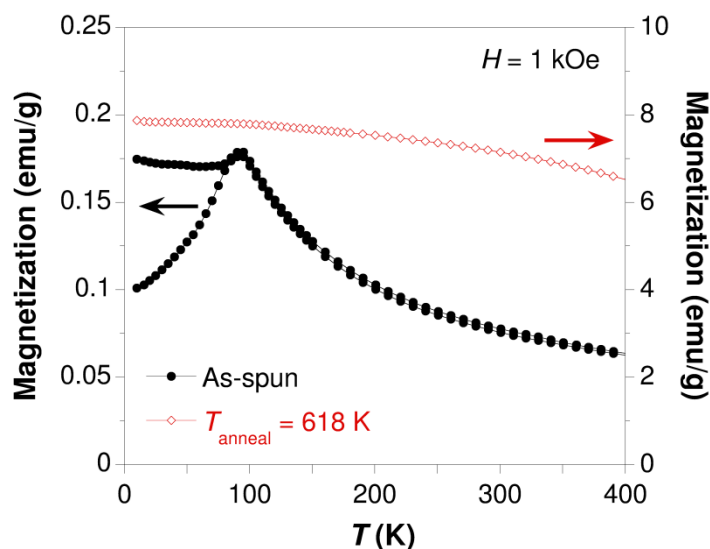
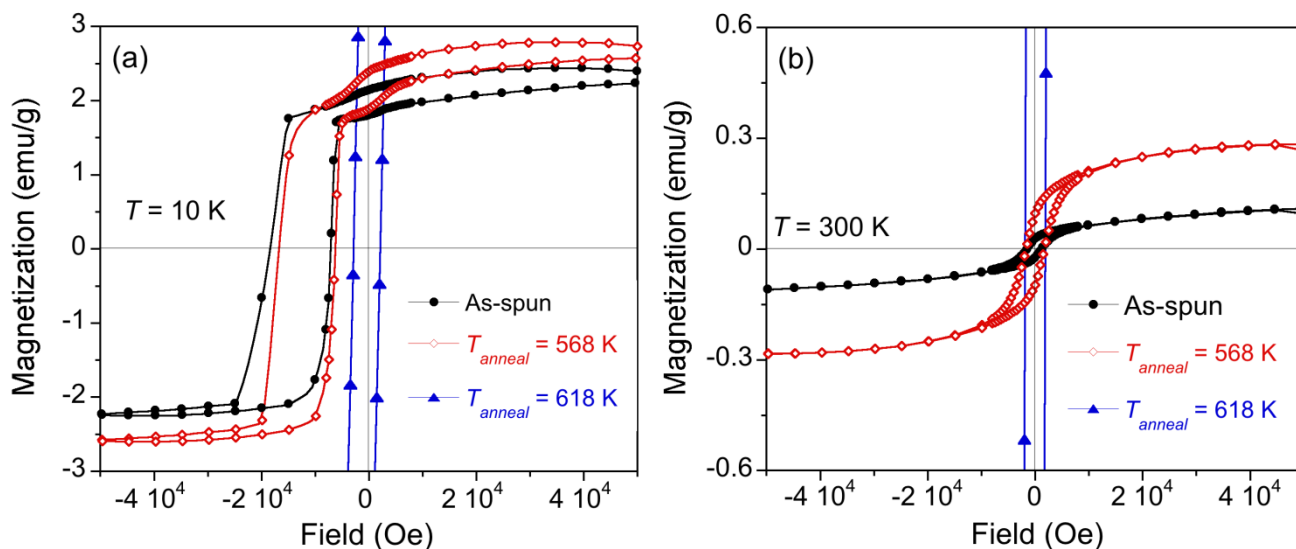


**Figure 4.** FC magnetization loops at (a)  $T = 10$  K and (b)  $T = 300$  K for as-spun  $Mn_{55}Al_{45}$  ribbons (filled circles) and those annealed at  $T_{\text{anneal}} = 568$  K (open diamonds) and  $T_{\text{anneal}} = 618$  K (filled triangles), showing presence of two magnetic phases. Ribbons treated at 618 K display  $M_s \sim 18$  emu/g.

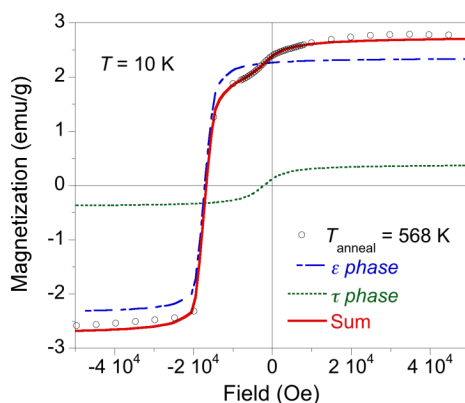


Finally, DSC data (presented in Figure 6c for discussion in Section 4) reveal a dominant exothermal peak centered at  $T = 654$  K, associated with the annealing-induced  $\varepsilon \rightarrow \tau$  transformation, although a more complex trace is observed in the lower temperature region, where an inflection point at around  $T \sim 550$  K is detected. The onset observed by DSC agrees with the evolution observed by magnetic characterization, revealing a higher sensitivity for small presence of emerging phases compared to X-ray diffraction results.

#### 4. Discussion

Analysis of the structural and magnetic data obtained from rapidly-solidified  $\text{Mn}_{55}\text{Al}_{45}$  ribbons provides insight into the evolution of the  $\varepsilon$ -phase to  $\tau$ -phase transformation in these nanostructured alloys. The as-quenched ribbons reveal metastable retention of the hexagonal (*hcp*)  $\varepsilon$ -MnAl phase, distributed into nanoscaled regions that are comparatively Mn-rich ( $\varepsilon_1$ ) and Mn-poor ( $\varepsilon_2$ ) upon rapid solidification from the melt [34]. Areas that are more concentrated in Mn contain a greater number of Mn-Mn nearest-neighbor pairs with AF character, while regions of lower Mn content contain more Mn-Mn next-nearest-neighbor pairs, with ferromagnetic character [36,37]. Strong interactions between these two regions lead to large exchange bias ( $H_{\text{ex}}$ ) values at  $T < T_{\text{peak}}$ , analogous to the reported mictomagnetic character of AgMn or CuMn alloys in which compositional fluctuations and strong coupling between Mn-rich and Mn-poor areas yield the formation of exchange-biased loops [36,38]. Employing the assumptions of an atomic radius for Al of  $\sim 1.25 \text{ \AA}$  and  $\sim 1.40 \text{ \AA}$  for Mn [39], and utilizing the calculated unit cell volumes of the  $\varepsilon_1$  and  $\varepsilon_2$  phases in the alloy (Section 3) obtained by X-ray diffraction, it is determined that the Mn-rich phase contains  $\sim 64 \pm 3 \text{ at.}\%$  Mn, whereas the Mn-poor phase contains  $\sim 60 \pm 3 \text{ at.}\%$  Mn, within the Mn content range for the  $\varepsilon$ -phase proposed by Liu *et al.*[40]. These high Mn concentrations, as compared to the nominal Mn content, are consistent with the coexistence of the  $\varepsilon$ -phases with the lower-Mn-content  $\gamma_2$ -phase of approximate composition 35–45 at.% Mn.

**Figure 5.** Modeling of the hysteretic demagnetization curve obtained at 10 K from  $\text{Mn}_{55}\text{Al}_{45}$  ribbons annealed at 568 K (open circles) into two magnetic phases (dashed lines), in accordance with Equation (1).



The fraction of magnetic phases produced upon annealing was determined in the MnAl ribbon from hysteresis loop measurements obtained at 10 K, according to Equation (1) with typical results illustrated in Figure 5. Two magnetic phase contributions are noted: the first contribution is attributed to the exchange-biased magnetization response, predominantly driven by the hexagonal  $\varepsilon$ -phase (labeled as  $x_{\varepsilon}$ ), and the second magnetic contribution is associated with the FM  $\tau$ -MnAl phase (denoted as  $x_{\tau}$ ). As the magnetic features are well defined at low temperature, data collected at 10 K were used to display the evolution of the coercivity  $H_{\text{ci}}$  and the relative phase fraction of each phase at 10 K, Figure 6a,b, respectively. The decrease of the exchange bias field  $H_{\text{ex}}$  and the coercivity  $H_{\text{ci}}$  noted for  $T_{\text{anneal}} \geq 473 \text{ K}$  (Figure 6a), along with the simultaneous increase in the magnetization of the  $\varepsilon$ -MnAl

phase, suggests a reduction of antiparallel spin arrangement between nearest neighbors of the *hcp*  $\epsilon$ -phase regions with annealing attributed to Mn homogenization in the alloy. The increased coercivity of the  $\tau$ -MnAl phase in the annealing temperature range  $T_{\text{anneal}} \approx 523\text{--}568$  K, reaching a stable value of  $H_{\text{ci}} \sim 0.25$  T ( $H_{\text{ci}} \sim 2.5$  kOe), could be attributed to higher anisotropy associated with improved chemical order of the tetragonal  $L1_0$  phase, as well as improved microstructural features.

The contribution of the  $\tau$ -phase ( $x_\tau$ ) grows at the expense of the  $\epsilon$ -phases ( $x_\epsilon$ ) at  $T_{\text{anneal}} \geq 568$  K, as confirmed by the  $T = 10$  K data trend (Figure 6b). Further treatment at  $T_{\text{anneal}} = 618$  K causes a precipitous rise in  $x_\tau$  from approximately 15% to 90% of the total magnetization. DSC data (Figure 6c) indicates the onset of phase transformation, by the inflection point at around  $T \sim 530\text{--}570$  K, right below the exothermal peak centered at  $T = 654$  K signaling the massive  $\epsilon \rightarrow \tau$  phase transformation, in agreement with the onset observed by magnetic examination. Assuming a room-temperature saturation magnetization value  $M_s \sim 98$  emu/g for the  $\tau$ -MnAl phase [3,12], it is estimated that the  $\tau$ -MnAl content increases from 0.08 wt. % to 0.28 wt. % upon annealing in the range  $T_{\text{anneal}} = 523\text{--}568$  K. Subsequent heat treatment at  $T_{\text{anneal}} = 618$  K causes a significant increase in the  $\tau$ -phase contribution from 0.28 wt. % to at least 18.0 wt. %, confirmed by the qualitative increase of magnetization featured by the alloy ( $M_s \sim 18$  emu/g) and the XRD evaluation of its crystallographic constituents. Based on the magnetic measurements, it can be concluded that nucleation of the  $\tau$ -MnAl phase seems to occur at  $T_{\text{anneal}} \approx 568$  K, around 100 K lower than previously-reported values for the onset of the  $\epsilon \rightarrow \tau$  transformation in quenched MnAl alloys, and similar to those observed in nanostructured samples, as summarized in Table 1. The significantly-reduced  $\tau$ -MnAl nucleation temperature confirmed in this work is thus attributed to the refined  $\epsilon$ -MnAl nanocrystalline structure and a large amount of crystal defects featured by rapid solidification via melt-spinning to directly obtain the  $\epsilon$ -MnAl parent phase, opening potential pathways to develop energy-efficient routes to fabricate MnAl permanent magnets.

**Figure 6.** Thermal evolution of (a)  $H_{\text{ci}}$  and (b) relative fraction of the hysteretic magnetization ( $x_i$ ) contributed by the  $\epsilon$ -MnAl phase regions and  $\tau$ -MnAl at 10 K, determined by Equation (1); dashed lines were drawn to guide eye; (c) DSC trace of as-spun  $\text{Mn}_{55}\text{Al}_{45}$  ribbon showing  $\tau$ -MnAl formation (Inset: first derivative of the DSC plot).

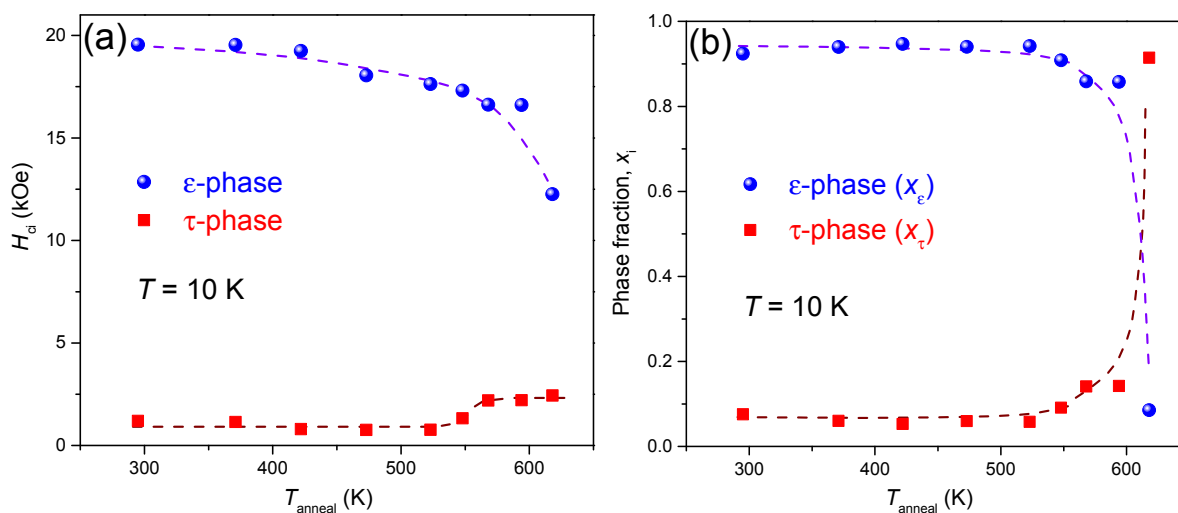
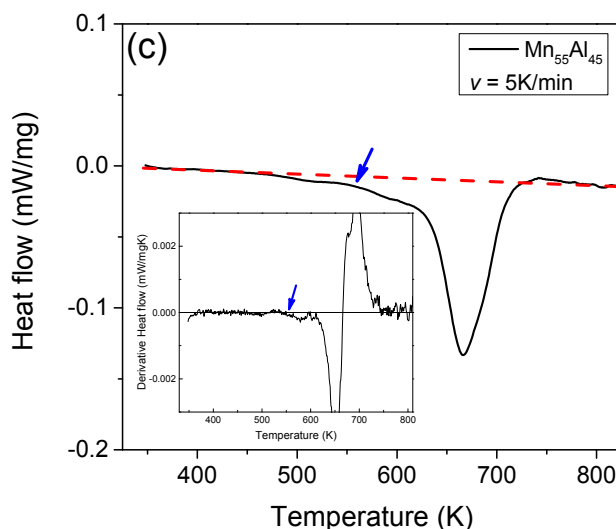


Figure 6. Cont.



**Table 1.** Reported initial formation temperature of the  $\tau$ -MnAl phase as a function of material processing method.

Fabrication/processing method	$\tau$ -MnAl formation temperature (K)	Method	References
Water-quenched Mn <sub>53</sub> Al <sub>46</sub> C <sub>2</sub>	723 K	Annealed	[23]
Oil-quenched Mn <sub>55</sub> Al <sub>45</sub>	800 K	Annealed	[13]
<i>Nonequilibrium synthesis methods</i>			
Splat-quenching	~700 K	DSC ( <i>onset</i> )	[20]
	723 K	DSC ( <i>peak</i> )	[20]
Mechanical milling	~600 K	DSC ( <i>onset</i> )	[28]
	665 K	DSC ( <i>peak</i> )	[28]
	623 K	XRD	[28]
Melt-spun Mn <sub>54</sub> Al <sub>44</sub> C <sub>2</sub> (at 25 m/s)	~725 K	DSC ( <i>onset</i> )	[27]
	779 K	DSC ( <i>peak</i> )	[27]
Melt-spun Mn <sub>55</sub> Al <sub>45</sub> (at 40 m/s)	748 K	<i>M(T)</i> curves	[27]
	~710 K	DSC( <i>onset</i> )	[19]
Melt-spun Mn <sub>55</sub> Al <sub>45</sub> (at 64 m/s)	758 K	DSC( <i>onset</i> )	[19]
	~550 K	DSC ( <i>onset</i> )	This work
	654 K	DSC ( <i>peak</i> )	This work
Melt-spun Mn <sub>55</sub> Al <sub>45</sub> (at 64 m/s)	618 K	XRD	This work
	568 K	<i>M(H)</i> curves	This work

## 5. Conclusions

This work provides insight into the phase transformation of rapidly-solidified nanostructured Mn<sub>55</sub>Al<sub>45</sub> alloys, from the metastable hexagonal  $\epsilon$ -phase to the  $L1_0$ -ordered  $\tau$ -phase, by means of detailed annealing procedures. The as-spun ribbons are confirmed to exhibit fluctuations in the local Mn content, causing phase separation into antiferromagnetic Mn-rich regions of the hexagonal  $\epsilon$ -MnAl phase and Mn-poor regions that possess ferromagnetic character; exchange interactions between these

regions result in large exchange bias shifts of approximately  $\sim 13$  kOe at  $T = 10$  K. Heat treatment at moderate temperatures ( $T_{\text{anneal}} \geq 473$  K) causes Mn diffusion and homogenization throughout the matrix, reducing the exchange bias effect. The  $\epsilon \rightarrow \tau$  transformation revealed by magnetic measurements starts after annealing at  $T_{\text{anneal}} \geq 568$  K (295 °C), signifying the onset of the tetragonal FM  $\tau$ -MnAl nucleation from the *hcp*  $\epsilon$ -MnAl parent phase at about 100 K lower than indicated by previous reports. The fine grains of the  $\epsilon$ -MnAl parent phase are thought to be responsible for this large reduction in transition temperature. Understanding the nature of the  $\epsilon \rightarrow \tau$  transformation could enable further reduction of the transformation temperature, which may play an impactful role for improving fabrication and processing techniques and strategies, and engineering of  $L1_0$ -type  $\tau$ -MnAl permanent magnets.

### Acknowledgments

This research has been funded by the Office of Naval Research (ONR), under the auspices of grant no. N00014-10-1-0553 and by ARPA-E Award# DE-AR0000186 (J.T.O.).

### Conflicts of Interest

The authors declare no conflict of interest.

### References

1. Lewis, L.H.; Jimenez-Villacorta, F. Perspectives on permanent magnetic materials for energy conversion and power generation. *Metall. Mater. Trans. A* **2013**, *44*, 2–20.
2. Coey, J.M.D. Permanent magnets: Plugging the gap. *Script. Mater.* **2012**, *67*, 524–529.
3. Park, J.H.; Hong, Y.K.; Bae, S.; Lee, J.J.; Jalli, J.; Abo, G.S.; Neveu, N.; Kim, S.G.; Choi, C.J.; Lee, J.G. Saturation magnetization and crystalline anisotropy calculations for MnAl permanent magnet. *J. Appl. Phys.* **2010**, *107*, 09A731.
4. Coey, J.M.D. Hard magnetic materials: A perspective. *IEEE Trans. Magn.* **2011**, *47*, 4671–4681.
5. Kharel, P.; Li, X.Z.; Shah, V.R.; Al-Aqtash, N.; Tarawneh, K.; Sabirianov, R.F.; Skomski, R.; Sellmyer, D.J. Structural, magnetic, and electron transport properties of MnBi:Fe thin films. *J. Appl. Phys.* **2012**, *111*, 07E326.
6. Yang, J.B.; Yang, Y.B.; Chen, X.G.; Ma, X.B.; Han, J.Z.; Yang, Y.C.; Guo, S.; Yan, A.R.; Huang, Q.Z.; Wu, M.M.; *et al.* Anisotropic nanocrystalline MnBi with high coercivity at high temperature. *Appl. Phys. Lett.* **2011**, *99*, 082505.
7. Kono, H. Ferromagnetic phase in manganese-aluminum system. *J. Phys. Soc. Jpn.* **1958**, *13*, 1444–1451.
8. Koch, A.J.J.; Philips, N.V.; Hokkeling, P.; v.d.Steeg, M.G.; de Vos, K.J. New material for permanent magnets on a base of Mn and Al. *J. Appl. Phys.* **1960**, *31*, 75S–77S.
9. Chen, T.; Stutius, W.E. The phase transformation and physical properties of MnBi and  $\text{Mn}_{1.08}\text{Bi}$  compounds. *IEEE Trans. Magn.* **1974**, *MAG-10*, 581.
10. Wyslocki, J.J.; Pawlik, P.; Przybyl, A. Magnetic properties of the non-oriented  $\epsilon$ -phase in Mn-Al-C permanent magnet. *Mater. Chem. Phys.* **1999**, *60*, 211–213.

11. Hoydick, D.P.; Palmiere, E.J.; Soffa, W.A. Microstructural development in MnAl-base permanent magnet materials: New perspectives. *J. Appl. Phys.* **1997**, *81*, 5624–5626.
12. Kamino, K.; Kawaguchi, T.; Nagakura, M. Magnetic properties of manganese-aluminum system alloys. *IEEE Trans. Magn.* **1966**, *MAG-2*, 506–510.
13. Kuo, P.C.; Yao, Y.D.; Huang, J.H.; Chen, C.H. Fabrication and magnetic properties of manganese-aluminum permanent magnets. *J. Magn. Magn. Mater.* **1992**, *115*, 183–186.
14. Le Breton, J.M.; Bran, J.; Folcke, E.; Lucis, M.; Larde, R.; Jean, M.; Shield, J.E. Structural modifications in a Mn<sub>54</sub>Al<sub>43</sub>C<sub>3</sub> melt-spun alloy induced by mechanical milling and subsequent annealing investigated by atom probe tomography. *J. Alloys Compd.* **2013**, *581*, 86–90.
15. Rama Rao, N.V.; Gabay, A.M.; Li, W.F.; Hadjipanayis, G.C. Nanostructured bulk MnBi magnets fabricated by hot compaction of cryomilled powders. *J. Phys. D* **2013**, *46*, 265001.
16. McCurrie, R.A.; Rickman, J.; Dunk, P.; Hawkrigde, D.G. Dependence of the permanent magnet properties of manganese-aluminum (Mn<sub>55</sub>Al<sub>45</sub>) on particle size. *IEEE Trans. Magn.* **1978**, *MAG-14*, 682–684.
17. Gutfleisch, O.; Willard, M.A.; Brück, E.; Chen, C.H.; Sankar, S.G.; Liu J.P. Magnetic materials and devices for the 21st century: Stronger, lighter, and more energy efficient. *Adv. Mater.* **2011**, *23*, 821–842.
18. Poudyal, N.; Liu, J.P. Advances in nanostructured permanent magnets research. *J. Phys. D* **2013**, *46*, 043001.
19. Liu, Z.W.; Chen, C.; Zheng, Z.G.; Tan, B.H.; Ramanujan, R.V. Phase transitions and hard magnetic properties for rapidly solidified MnAl alloys doped with C, B, and rare earth elements. *J. Mater. Sci.* **2012**, *47*, 2333–2338.
20. Kim, Y.J.; Perepezko, J.H. Formation of a metastable ferromagnetic  $\tau$  phase during containerless melt processing and rapid quenching in manganese-aluminum-carbon alloys. *J. Appl. Phys.* **1992**, *71*, 676–680.
21. Crew, D.C.; McCormick, P.G.; Street, R. MnAl and MnAlC permanent magnets produced by mechanical alloying. *J. Appl. Phys.* **1995**, *32*, 315–318.
22. Rao, V.; Pramanik, S.; Tewari, C.R.; Singh, S.R.; Mohanty, O.N. Phase transformations in manganese-aluminum permanent magnet alloys. *J. Mater. Sci.* **1989**, *24*, 4088–4093.
23. Dobromyslov, A.V.; Ermakov, A.E.; Taluts, N.I.; Uimin, M.A. Electron microscopy investigation of phase transformations in manganese-aluminum-carbon alloy. *Phys. Status Solidi A* **1985**, *88*, 443–454.
24. Kim, Y.J.; Perepezko, J.H. The thermodynamics and competitive kinetics of metastable  $\tau$  phase development in manganese-aluminum-base alloys. *Mater. Sci. Eng. A* **1993**, *A163*, 127–134.
25. Yanar, C.; Wiezorek, J.M.K.; Radmilovic, V.; Soffa, W.A. Massive transformation and the formation of the ferromagnetic L10 phase in manganese-aluminum-based alloys. *Metall. Mater. Trans. A* **2002**, *33A*, 2413–2423.
26. Duan, C.Y.; Qiu, X.P.; Ma, B.; Zhang, Z.Z.; Jin, Q.Y. The structural and magnetic properties of  $\tau$ -MnAl films prepared by Mn/Al multilayers deposition plus annealing. *Mater. Sci. Eng. B* **2009**, *162*, 185–188.
27. Fazakas, E.; Varga, L.K.; Mazaleyrat, F. Preparation of nanocrystalline Mn-Al-C magnets by melt spinning and subsequent heat treatments. *J. Alloys Compd.* **2007**, *434–435*, 611–613.

28. Zeng, Q.; Baker, I.; Cui, J.B.; Yan, Z.C. Structural and magnetic properties of nanostructured Mn-Al-C magnetic materials. *J. Magn. Magn. Mater.* **2007**, *308*, 214–226.
29. Novak, G.A.; Colville, A.A. A Practical interactive least-squares cell-parameter program using an electronic spreadsheet and a personal-computer. *Amer. Miner.* **1989**, *74*, 488–490.
30. Patterson, A.L. The Scherrer formula for X-ray particle-size determination. *Phys. Rev.* **1939**, *56*, 978–982.
31. Bozorth, R.M.; Chapin, D.M. Demagnetizing factors of rods. *J. Appl. Phys.* **1942**, *13*, 320–326.
32. Stearns, M.B.; Cheng, Y. Determination of para- and ferromagnetic components of magnetization and magnetoresistance of granular Co/Ag films. *J. Appl. Phys.* **1994**, *75*, 6894–6899.
33. Predel, B. Al-Mn (Aluminum-Manganese). In *Landolt-Bornstein—Group IV Physical Chemistry*; Madelung, O., Ed.; Springer Materials: Berlin, Germany, 2013.
34. Jimenez-Villacorta, F.; Marion, J.L.; Sepehrifar, T.; Daniil, M.; Willard, M.A.; Lewis, L.H. Exchange anisotropy in the nanostructured MnAl system. *Appl. Phys. Lett.* **2012**, *100*, 112408.
35. Wyslocki, J.J.; Pawlik, P.; Przybyl, A. Magnetic properties of the non-oriented  $\epsilon$ -phase in Mn-Al-C permanent magnet. *Mater. Chem. Phys.* **1999**, *60*, 211–213.
36. Kouvel, J.S. The ferromagnetic-antiferromagnetic properties of copper-manganese and silver-manganese alloys. *Phys. Chem. Solids* **1961**, *21*, 57–70.
37. Kouvel, J.S. Exchange anisotropy in Cu-Mn and Ag-Mn alloys. *J. Appl. Phys.* **1960**, *31*, 142S–147S.
38. Jiménez-Villacorta, F.; Marion, J.L.; Sepehrifar, T.; Lewis, L.H. Tuning exchange anisotropy in nanocomposite AgMn alloys. *J. Appl. Phys.* **2012**, *111*, 07E141.
39. Slater, J.C. Atomic radii in crystals. *J. Chem. Phys.* **1964**, *41*, 3199.
40. Liu, X.J.; Kainuma, R.; Ohtani, H.; Ishida, K. Phase equilibria in the Mn-rich portion of the binary system Mn-Al. *J. Alloys Compd.* **1996**, *235*, 256–261.

© 2014 by the authors; licensee MDPI, Basel, Switzerland. This article is an open access article distributed under the terms and conditions of the Creative Commons Attribution license (<http://creativecommons.org/licenses/by/3.0/>).